The Astrophysical Journal, 715:1566–1574, 2010 June 1
doi:10.1088/0004-637X/715/2/1566

A TWISTED FLUX ROPE AS THE MAGNETIC STRUCTURE OF A FILAMENT IN ACTIVE REGION 10953 OBSERVED BY *HINODE*

A. Canou[1] and T. Amari[1,2]
[1] CNRS, Centre de Physique Théorique de l'Ecole Polytechnique, F-91128 Palaiseau Cedex, France; canou@cpht.polytechnique.fr
[2] Observatoire de Paris, LESIA, 5 place Jules Janssen, F-92190 Meudon Cedex, France
Received 2010 February 8; accepted 2010 April 19; published 2010 May 12

ABSTRACT

The presence of twisted flux ropes (TFRs) in pre-eruptive/flaring magnetic configurations is of main interest for our understanding of the structure and dynamics of the solar corona. On the one hand, their presence is a key ingredient in several theoretical models for the magnetic support of material in filaments, or triggering of coronal mass ejections as well as the emergence of structures from the convection zone into the corona. On the other hand, several observations have shown the presence of twist and shear during eruptive and flaring phases of eruptive phenomena. In this paper, we consider the determination of the magnetic structure of active region (AR) 10953 observed by *Hinode* and reconstructed using our two nonlinear force-free models. We show that the reconstructed magnetic configurations exhibit a TFR along the southern part of the neutral line. Moreover, the location of the magnetic dips within the TFR agrees within a good level of accuracy with the Hα images taken by *SMART* and the vertically integrated current density recovers the main structure present in *Hinode*/XRT images. The free magnetic energy is also found to be large enough to power the two C-class flares of the following days. We finally compare our results with those of Su et al. who proposed an interesting model of the same AR in which a TFR is inserted at the same location using the flux rope insertion method.

Key words: magnetic fields – magnetohydrodynamics (MHD) – Sun: corona – Sun: filaments, prominences

Online-only material: color figures

1. INTRODUCTION

Large-scale eruptive phenomena such as flares and coronal mass ejections (CMEs) happen in solar corona above and in the neighborhood of active regions (ARs). Although the mechanisms which trigger these phenomena are not precisely yet understood, the magnetic field is known to play a major role. From our current understanding, the energy is stored in the magnetic field through the electrical currents flowing in the corona during the slow evolution of the AR. The magnetic energy is then released during flares; sometimes with the trigger of CMEs.

Several observational studies have shown the presence of shear and twist during flaring and eruptive phases, stressing the fact that the magnetic field is far from the current-free state (or potential state). A famous example of twist can be seen in the well-known Grandaddy eruptive prominence. And Gary & Moore (2004) clearly presented evidence for the presence of twist during the eruptive phase of an AR filament. However, observations have never been able to show clearly and without ambiguity the existence of twisted flux ropes (TFRs) in equilibrium in pre-eruptive magnetic configurations.

To model those observations, two generic classes of magnetic structure have been proposed: the TFR model which presents twist and shear, and the magnetic arcade model which presents only shear, although the definition and distinction between twist and shear in three-dimensional (3D) configurations is not obvious for a slightly twisted configuration. We do not intend to review the TFR model in the context of the solar prominences modeling (see Démoulin 1998; Mackay et al. 2010); but we recall that it has first been studied in the two-dimensional (2D) potential field (e.g., Kuperus & Raadu 1974; Anzer & Priest 1985) and the linear force-free field (e.g., Amari & Aly 1989, 1992; Démoulin & Priest 1988, 1989), and it was shown to possess dips and present the inverse configuration polarity. Later on, 3D axysymetric models have been developed (e.g., Aulanier & Demoulin 1998; Titov & Démoulin 1999), and the role of flux cancellation in creating such TFRs has been highlighted (van Ballegooijen & Martens 1989; Amari et al. 1999). Since then, filament located on the disk has been numerically modeled (e.g., Lionello et al. 2002; van Ballegooijen 2004; Dudík et al. 2008). On the other hand, the magnetic arcade model has also been shown to possess dips and is thus another possible candidate for the support of matter in the magnetic field (DeVore & Antiochos 2000; Aulanier et al. 2002).

Moreover, both classes of models have also been shown to lead to large-scale eruptions during magnetohydrodynamic (MHD) evolution. While TFR models can lead to disruptions either in simple background topology (e.g., Amari et al. 2000, 2003a, 2003b; Aulanier et al. 2010, and references therein) or in a complex one (Amari et al. 2007), the arcade model requires a complex background topology. A TFR is then created by reconnection at the null point only during the eruptive phase (e.g., Antiochos et al. 1999; Lynch et al. 2008).

Furthermore, numerical simulations of emergence of magnetic structures through the solar convection zone (CZ) and/or across the photosphere have been given a great deal of attention in recent years. Assuming the presence of a TFR in the CZ and studying the rise of this structure, those calculations have reproduced several AR features such as the characteristic tongues (López Fuentes et al. 2000; Fan 2001) and have been shown to lead to the eruption of the emerging coronal structure when the initial underlying TFR possesses a sufficient amount of twist (Magara & Longcope 2003; Fan & Gibson 2004; Amari et al. 2004, 2005; Archontis et al. 2004; Galsgaard et al. 2005; Manchester et al. 2004; Cheung et al. 2007). However, all those results assume the presence of a TFR either in the CZ or in the corona prior to the eruption, and the issue of the pre-existence of TFRs as stable structures in the corona remains to be addressed.

For that purpose, the determination of the coronal magnetic configuration still turns out to be of principal interest to prove or disprove one or the other model regardless of the AR under study.

A possible answer to that issue can be given by solving the *reconstruction problem* which has become a major topic of research in the past decades (Amari et al. 1997; Schrijver et al. 2006; Aly & Amari 2007; Wiegelmann 2008). Assuming the low corona to be in a force-free state due to the low-β value in the coronal plasma, the aim is to reconstruct the 3D magnetic configuration using the vector magnetogram measured near the photospheric level by vector magnetographs (e.g., *THEMIS*/MTR, *SOLIS*/VSM, *MSO*/IVM, *Hinode*/SOT/SP). Although this approach in its globality is subject to numerous assumptions and uncertainties (e.g., measurement errors, inversion of Stokes parameters, resolution of the 180° ambiguity, photosphere not perfectly force-free; see McClymont et al. 1997) mixed with a complex mathematical problem, some quite interesting results in favor of the TFR model have been provided. For instance, Régnier & Amari (2004) and Guo et al. (2010) showed the presence of a TFR as the magnetic structure supporting a filament respectively in AR 8151 and AR 10767, whereas Canou et al. (2009) highlighted the presence of a TFR tangent to the photosphere in the emerging main spot of AR 10808.

This paper considers the NOAA AR 10953 which is known to present good clues as to the emergence of a TFR related to the modification of the shape of a filament (see Section 2). We applied the two reconstruction methods XTRAPOL and FEMQ (Amari et al. 2006) within the framework of the previous study performed by DeRosa et al. (2009), and we found the presence of a TFR without any assumption other than that the corona is force-free. We extend this previous work within a more detailed study of the configuration as well as its link with the physics of the AR. In Section 2, we recall the context of this study and Section 3 presents the reconstruction method. The results are shown in Section 4 and are compared to the study of Su et al. (2009) in Section 5. The conclusion comes in Section 6.

2. CONTEXT

AR 10953 was a rather simple bipolar AR, formed by a strong concentration of negative polarity as leading sunspot and by a less concentrated positive polarity as following sunspot. AR 10953 did not have a strong flare activity. Only two small flares occurred during its appearance: a C8.5 two-ribbon flare on 2007 May 2 at 23:28 UT and a C4.2 flare on 2007 May 5 at 12:20 UT. Otherwise, the region was flare quiet above the C1.0 level. An interesting filament, on which we will focus later in the paper, extended from the main negative polarity to the south of the AR 10953. It was present from before 2007 April 28 until after May 4 even though its shape changed and that it suffered several activations. By studying the temporal evolution of vector magnetograms, Okamoto et al. (2008) suggested that a TFR emerged from below the photosphere. Moreover, Okamoto et al. (2009) studied with multi-instrument observations the formation and the maintenance of the filament. They related it to the emergence of the TFR. On the other hand, Su et al. (2009) used the flux rope insertion method (van Ballegooijen et al. 2007; Bobra et al. 2008) to model the magnetic structure of the filament before the C8.5 flare on May 2.

In this paper, we use the same data sets as those described in DeRosa et al. (2009) about which we recall some details. These were taken from a scan of the Spectro-Polarimeter (SP) instrument of the Solar Optical Telescope (SOT; Tsuneta et al. 2008) on board *Hinode* on 2007 April 30 from 22:30 to 23:00 UT. At this moment, AR 10953 was located at S10E09. The 180° ambiguity was solved using the AZAM utility (Metcalf et al. 2006, and references therein). Since the magnetic field is not perfectly force-free on the photosphere, the data were preprocessed by the method of Wiegelmann et al. (2006). This procedure decreases the magnetic forces and torques (Aly 1989) and reduces the small-scale variations of the magnetic field by a smoothing operation. It is also worth noting that the data from *Hinode*/SOT/SP just cover the central part of the AR and thus the vector magnetogram has been embedded in the line-of-sight magnetogram from the Michelson Doppler Imager (MDI; Scherrer et al. 1995) on board the *Solar and Heliospheric Observatory* spacecraft. However, no information about the transverse field for the MDI magnetogram exists. The final vector magnetogram presents a field of view of 186 × 186 Mm^2 with a resolution of 320 × 320 pixels.

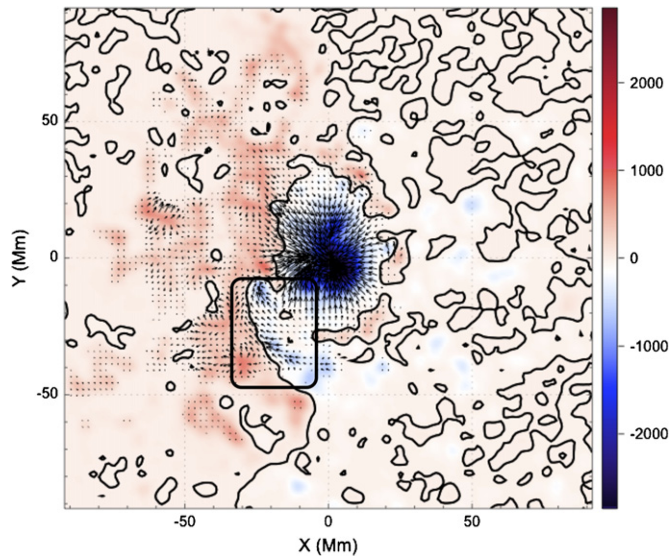

Figure 1. Preprocessed vector magnetogram from *Hinode*/SOT/SP on 2007 April 30 at 23:00 UT. The black contour represents the PIL, and the transverse magnetic field vectors below $||\mathbf{B}_t|| < 30$ G are not plotted.

(A color version of this figure is available in the online journal.)

Figure 1 shows the preprocessed vector magnetogram of the AR. In the black box along the southern part of the polarity inversion line (PIL), arrows representing the transverse magnetic field point from the negative polarity to the positive one; this particular configuration is referred to as T-like topology feature (Aly & Amari 1989) or bald patches (Titov et al. 1993) when seen on the photosphere and as inverse polarity configuration when seen higher in the corona. It indicates the presence of field lines tangent to the photosphere with an upward concavity suggesting the presence of a TFR; this location also corresponds to the projection on a plane parallel to the photosphere of the filament location. The scan of *Hinode*/SOT/SP was done one day after the filament changed from a complex shape to a simpler one (Okamoto et al. 2009). It also corresponds to a period of about two days before the study of Su et al. (2009) and during it, the flare activity was much below the C1.0 level.

3. RECONSTRUCTION METHOD

The corona $\Omega = \{z > 0\}$ is supposed to be filled up with a low-β plasma. The magnetic field is thus in a force-free state which fulfills the following set of equations:

$$\nabla \times \mathbf{B} = \alpha(\mathbf{r})\mathbf{B} \tag{1}$$

$$\nabla \cdot \mathbf{B} = 0 \tag{2}$$

$$\mathbf{B} \cdot \nabla\alpha(\mathbf{r}) = 0, \tag{3}$$

where α is called the force-free function and, in the case of a nonlinear force-free (NLFF) field, it depends on the position. Equation (1), which states that the electric current density $\mathbf{j}$ is collinear to the magnetic field $\mathbf{B}$, just expresses the balance between the magnetic tension and pressure forces. Equation (2) is the well-known divergence-free condition. Equation (3) (derived from the divergence of Equation (1)) means that α is constant along each field lines.

To solve this boundary value problem, we used two different methods: XTRAPOL and FEMQ (Amari et al. 2006). Both are based on a Grad–Rubin algorithm (Grad & Rubin 1958), which iteratively solves the hyperbolic and elliptic parts of the above set of equations with the appropriate boundary conditions (BCs), and which is associated with a well-posed formulation

$$\mathbf{B}^{(n)} \cdot \nabla\alpha^{(n)} = 0 \qquad \text{in} \quad \Omega \tag{4}$$

$$\alpha^{(n)} = \alpha_{\rm phot} \quad \text{on} \quad \partial\Omega^{+} \text{ or } \partial\Omega^{-}, \tag{5}$$

and

$$\nabla \times \mathbf{B}^{(n+1)} = \alpha^{(n)}\,\mathbf{B}^{(n)} \quad \text{in} \quad \Omega \tag{6}$$

$$\nabla \cdot \mathbf{B}^{(n+1)} = 0 \qquad \text{in} \quad \Omega \tag{7}$$

$$B_n^{(n+1)} = B_{z,\rm phot} \qquad \text{on} \quad \partial\Omega. \tag{8}$$

In the previous equations, the superscript n represents the nth iteration of the Grad–Rubin algorithm. Equations (5) and (8) are the BCs for the hyperbolic and elliptic parts of the system, respectively. They are provided on the lower boundary $\partial\Omega = \{z = 0\}$ which is assumed to correspond to the photospheric layer where the vector magnetogram is measured. Moreover, Equation (5) means that $\alpha_{\rm phot}$ is specified either in the positive polarity $\partial\Omega^{+}$ where $B_n > 0$, or in the negative polarity $\partial\Omega^{-}$ where $B_n < 0$. In both these methods, the Grad-Rubin algorithm is initialized with a potential field $\mathbf{B}^{(0)} = \mathbf{B}_\pi$ (also called current-free field) associated with $\alpha^{(0)} = 0$ in Equations (4)–(8) although their lateral and top BCs are different.

3.1. Two Different Implementations

The main properties of these two methods are briefly recalled; the interested reader is referred to Amari et al. (2006) for a detailed explanation.

1. XTRAPOL. This method is based on a finite difference discretization scheme and solves Equation (4)–(8) with the vector potential representation for the magnetic field ($\mathbf{B} = \nabla \times \mathbf{A}$) along with a specific gauge condition. The different operators are discretized on a nonuniform and staggered mesh with Cartesian coordinates such that the divergence-free condition is thus satisfied to machine accuracy.
2. FEMQ. This method does not lead to exactly divergence-free solution. It is based on a Q1 finite element scheme; the force-free equations are solved for the magnetic field $\mathbf{B}$ and not for the vector potential. The divergence-free condition is addressed by minimizing $\nabla \cdot \mathbf{B}$ in the least square sense for the associated div-curl system corresponding to the elliptic problem.

3.2. Generation of Boundary Conditions

Both methods require the z-component of the magnetic field and the force-free function $\alpha_{\rm phot}$ on $\partial\Omega$. Whereas $B_{z,\rm phot}$ is directly accessible from the vector magnetogram, $\alpha_{\rm phot}$ needs to be computed as follows by assuming that the vector magnetogram is force-free:

$$\alpha_{\rm phot} = \frac{j_{z,\rm phot}}{B_{z,\rm phot}} = \frac{1}{\mu_0}\frac{(\nabla \times \mathbf{B}_{\rm phot})_z}{B_{z,\rm phot}}, \tag{9}$$

where $j_{z,\rm phot}$ is the vertical component of the current density.

From Equation (9), one can see that special treatment is needed near the PIL where $B_{z,\rm phot}$ is small. As in Bleybel et al. (2002), Régnier & Amari (2004), and Canou et al. (2009), we choose to set $\alpha_{\rm phot}$ to zero where $|B_{z,\rm phot}|$ is below its measurement error. A similar cutoff value is used for $||\mathbf{B}_t||$ in order to avoid unreliable values of $j_{z,\rm phot}$ due to sudden variations of $\mathbf{B}_t$ below the noise level. Further smoothing, interpolation on the computational mesh, or reconstruction could restore on the PIL some nonzero value of $\alpha_{\rm phot}$ taken from the vicinity of the PIL. The maps of $B_{z,\rm phot}$, $j_{z,\rm phot}$, and $\alpha_{\rm phot}$ are shown in Figure 2. It should be noted that the data have not been smoothed in this particular case since they were already preprocessed and smoothed using the method of Wiegelmann et al. (2006).

The normal component of the vector magnetogram presents a slight flux imbalance of 1.5% on the photosphere ($\phi^{+} = 1.67 \times 10^{22}$ Mx and $\phi^{-} = -1.62 \times 10^{22}$ Mx). We use open BCs so that the magnetic flux is balanced (up to round-off machine errors) for all the boundaries of our simulation domain, and field lines are allowed to connect with the lateral and top boundaries.

4. RESULTS AND INTERPRETATION

The magnetic field is reconstructed in a volume of $[-93\,;93] \times [-93\,;93] \times [0\,;149]$ Mm^3 discretized on a nonuniform mesh in which gridpoints are accumulated in the areas where current is stronger, with $180 \times 160 \times 120$ gridpoints for both XTRAPOL and FEMQ models. The cutoff values are 5 G for $|B_{z,\rm phot}|$ and 30 G for $||\mathbf{B}_t||$. The mesh and the BCs are the same for both models and are shown in Figures 2(a) and 2(c).

4.1. Magnetic Configurations and Presence of a TFR

Global views of the magnetic configuration are shown in Figure 3: panels (a) and (c) for XTRAPOL and panels (b) and (d) for FEMQ. A TFR clearly appears above the southern part of the PIL as suggested by Okamoto et al. (2008, 2009). Above the TFR, the presence of weakly sheared loops participates in the relative confinement (and thus stability properties) of the magnetic system. Hereafter, we will mainly focus on the results obtained with XTRAPOL; yet we found very similar results with the reconstruction obtained with FEMQ.

As shown in Figure 4, the TFR reconstructed with XTRAPOL is visible in a closer view. Three different sets of field lines are drawn: the darker one represents the twisted core of the TFR, the purple one is highly sheared but little twisted, and the green one is low-lying short and sheared arcades. The horizontal transition between the short arcades (green set) and the long one (purple set) induces the presence of rapid variation in the connectivity mapping defined by the field lines, resulting in the presence of two quasi-separatrix layers (Titov et al. 2002) on each side of

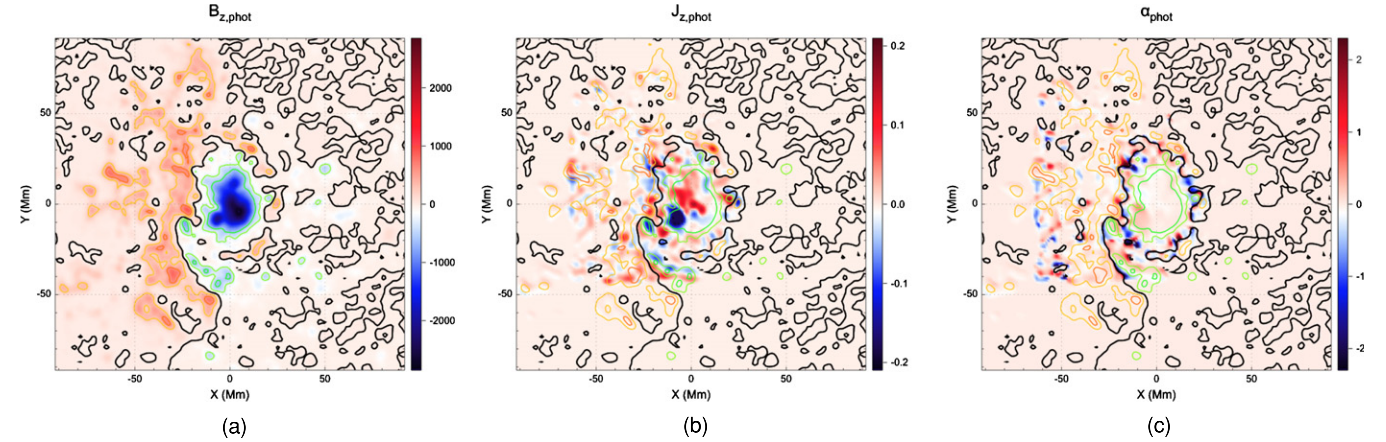

Figure 2. (a) Vertical component $B_{z,\mathrm{phot}}$ of the magnetic field in Gauss. (b) Vertical component $j_{z,\mathrm{phot}}$ of the current density in mA cm^{-2}. (c) α_{phot} function in Mm^{-1}. The black contours represent the PIL, and the colored ones are $B_{z,\mathrm{phot}} = \pm 300, \pm 600$ G.

(A color version of this figure is available in the online journal.)

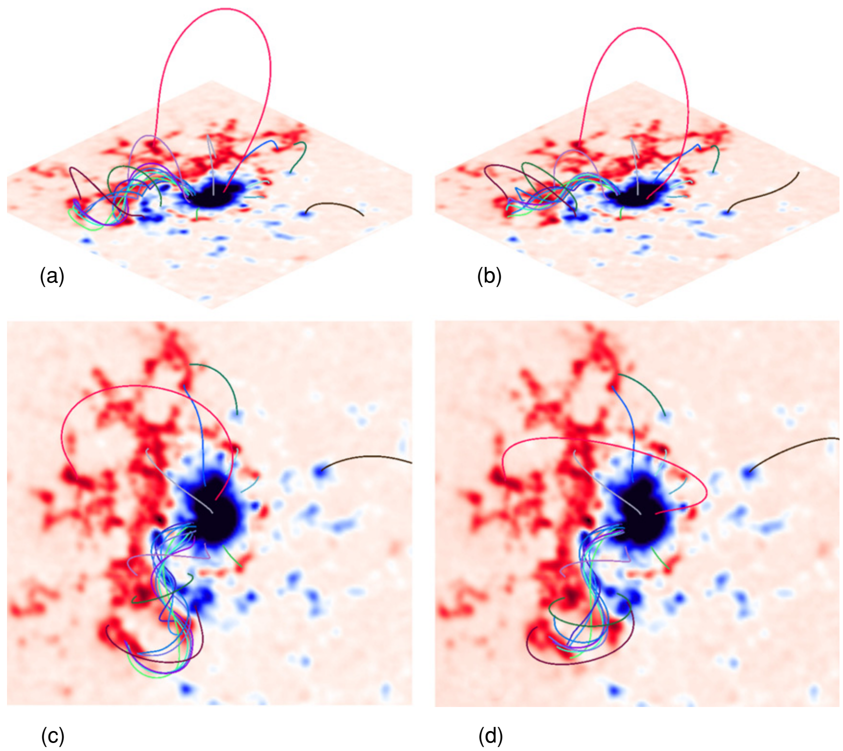

Figure 3. Same selected field lines are drawn for each model: (a) global view of AR 10953 reconstructed by XTRAPOL, (b) same as (a) but reconstructed with FEMQ, (c) view from above for XTRAPOL, and (d) same as (c) but for FEMQ.

(A color version of this figure is available in the online journal.)

the PIL. Those structures form a hyperbolic flux tube which surrounds the twisted core (Titov 2007). It is to be noted that there is no null point between the low-lying sheared arcades and the TFR.

In the negative polarity, the footpoints of the TFR core are anchored where the large amount of vertical current density is responsible for its appearance (see Figure 2(b)). It should be noted that α_{phot} has been imposed in the negative polarity, on the one hand, to take into account this large amount of current and, on the other hand, to reduce the impact of the absence of information about the transverse magnetic field in the MDI data for the southern part of the AR.

In the positive polarity, the footpoints are anchored in two different locations separated by a negative polarity area (see Figures 2(a) and 4(a)). The height of the TFR is 25 Mm, it has a width of 15 Mm in its center, and a length of 78 Mm.

4.2. Remarks on Small Sheared Arcades below the TFR

As shown in Figure 4 for the XTRAPOL model, some small sheared arcades are present below the TFR; these are also present for FEMQ. But this presence is not expected and field lines tangent to the photosphere should rather be seen, in agreement with the BPs observed at this location on the vector magnetogram (Figure 1). The arcades extend on approximately two gridpoints (2.08 Mm) on each side of the PIL and extend vertically on about three gridpoints (0.62 Mm). We think that their presence is an artifact primarily caused by observational and thus associated computational reasons.

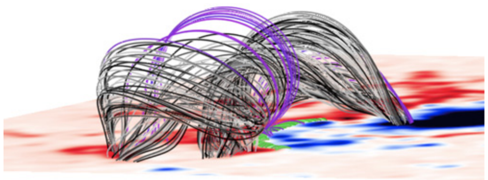

(a)

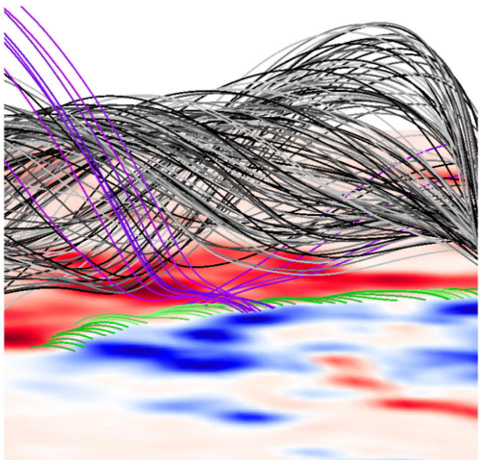

(b)

Figure 4. Zoom on the TFR: (a) its general shape (b) its central part. The same three set of field lines are drawn for both panels: green one, underlying sheared arcades; purple one, strongly sheared but few twisted field lines; and darker one, highly twisted core of the TFR.

(A color version of this figure is available in the online journal.)

As said in Section 3.2, the transverse magnetic field is unknown for most of the MDI data although the preprocessing of data restored some information. Thus, for the very southern part of the TFR, $\alpha_{\rm phot}$ is zero in both polarities.

Furthermore and despite the preprocessing, this data set presents an inconsistency with the force-free assumption. On the photosphere, one can write

$$\mathbf{j}_{\rm phot} = \alpha_{\rm phot}\mathbf{B}_{\rm phot}, \tag{10}$$

if $\mathbf{B}_{\rm phot}$ is assumed to be force-free. The point is that the usually used relation Equation (9) is only the projection of this equation: $j_{z,\rm phot} = \alpha_{\rm phot} B_{z,\rm phot}$. Equation (10) readily implies that for $\alpha_{\rm phot}$ bounded (a condition anyway necessary to ensure the existence of a solution, see Boulmezaoud & Amari 2000), the vertical current density should be null on the PIL. But one can see in Figure 2(b) that the current density differs from zero on the PIL, which therefore prevents the use of a l'Hospital rule as in Cuperman et al. (1991). Whether the breakdown of the force-free assumption may result from the emergence of the TFR and the presence of non-null magnetic forces linked to the presence of other forces (e.g., pressure gradient, plasma velocities near or higher than the Alfvèn velocity) is an issue that remains beyond the scope of the present study and is not solved in this paper.

However, it is worth noting that computing $\alpha_{\rm phot}$ directly from Equation (10) would avoid any constraint on the PIL (except only the presence of a null point) since $\alpha_{\rm phot}$ would be given by

$$\alpha_{\rm phot} = \frac{\mathbf{j}_{\rm phot} \cdot \mathbf{B}_{\rm phot}}{\mathbf{B}_{\rm phot} \cdot \mathbf{B}_{\rm phot}}\,. \tag{11}$$

Using Equation (11) might highly improve the efficiency of the Grad–Rubin-like reconstruction model. However, vector magnetograms should be given at two different heights in order to compute the transverse current density $\mathbf{j}_{t,\rm phot}$.

Table 1
Energies, Relative Helicity, and Force-Free Parameters for the Different Models

Model	W_π	$W\,[\mathbf{B}]$	ΔW	W_σ	ΔH	CWsin	$\langle\lvert f_i\rvert\rangle$
FEMQ	8.85	11.25	2.40	15.81	$\cdots$	0.10	2.06×10^{-4}
XTRAPOL	8.63	11.27	2.64	15.81	1.49	0.08	0.30×10^{-9}
Relaxed XTRAPOL	8.63	11.24	2.61	15.81	1.44	0.01	7.84×10^{-9}

Note. Energies are expressed in 10^{32} erg and helicities in 10^{42} G^2 cm^4 (see the text for details).

4.3. Magnetic Energy and Relative Helicity

The magnetic energy is defined as $W\,[\mathbf{B}] = \int_\Omega \frac{B^2}{2\mu_0}\,dV$. Various relevant magnetic energies have been computed for the two reconstruction methods and are summarized in the first two rows of Table 1. W_π, $W\,[\mathbf{B}]$, and W_σ are respectively the potential field, the NLFF field, and the open-field energies, and ΔW is the free magnetic energy, that is, the maximum energy that can be released during a flare and/or a CME.

Since the mesh and the distribution of $B_{z,\rm phot}$ are the same for XTRAPOL and FEMQ, the open-field energies are identical for both methods. But, as said in Section 3, the potential field was computed with two different lateral and top BCs, so that a small difference appears in the potential field energies.

The NLFF energies are very similar for both methods, and the configurations stored enough free energy to power the C-class flares. Nonetheless, as expected, the XTRAPOL model has a free magnetic energy ($0.31 \times W_\pi$) larger than that of the FEMQ model ($0.27 \times W_\pi$). This is due to the difference in their potential magnetic energies. It is also worth noting that, for both models, the Aly–Sturrock conjecture is clearly satisfied: $W_\pi \leqslant W\,[\mathbf{B}] < W_\sigma$ (Aly 1991; Sturrock 1991).

The relative magnetic helicity can easily be computed for XTRAPOL which solves the vector potential $\mathbf{A}$. Using the expression $\Delta H_m = \int_\Omega (\mathbf{A} + \mathbf{A}_\pi)\cdot(\mathbf{B} - \mathbf{B}_\pi)\,dV$ (Finn & Antonsen 1985), one gets a positive value for the relative helicity (see Table 1). For this southern AR, this is in agreement with the fact that southern ARs tend to have a positive helicity (and northern ARs a negative one; Pevtsov et al. 1995, 2001).

4.4. Quality of the Reconstruction and MHD Relaxed State

The last two columns of Table 1 present two parameters often used to indicate a measure of the quality of a reconstruction procedure. $\langle\lvert f_i\rvert\rangle$ represents a measure of the divergence-free condition and CWsin is the current-weighted average of the sine of the angle between the current density and the magnetic field (as defined in Wheatland et al. 2000). These two parameters are equal to zero for an exact force-free magnetic field. We found that these parameters are small enough for both models. Furthermore, whereas CWsin is almost identical to the one computed in DeRosa et al. (2009) with our models, $\langle\lvert f_i\rvert\rangle$ is even several orders of magnitude smaller. Indeed, our previous results were interpolated on a different mesh to facilitate the comparison and exploitation of the results. Thus, the benefit of using a staggered grid and of the minimization was lost for XTRAPOL and FEMQ models, respectively, while implying better values for the divergence of the magnetic field in this paper.

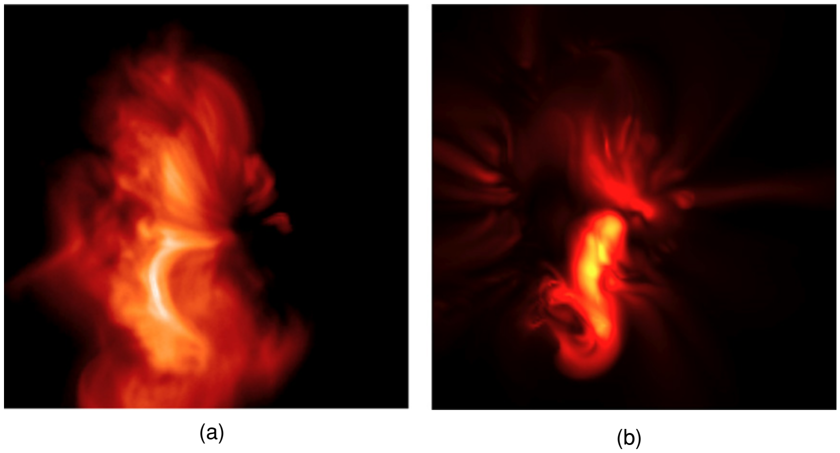

Figure 5. Qualitative comparison between *Hinode*/XRT images and the vertically integrated current density. (a) Time-averaged and logarithmically scaled *Hinode*/XRT soft X-ray image on 2007 April 30 between 22:30 and 23:00 UT. (b) Vertically integrated current density from XTRAPOL. The same field of view is plotted for both panels.

(A color version of this figure is available in the online journal.)

The magnetic configuration computed above as an NLFF model represents an equilibrium to a relatively good level of accuracy. This equilibrium may be either linearly stable or unstable. While there is no general necessary condition for the linear stability of a 3D force-free magnetic configuration in equilibrium having its footpoints connected to the boundary, there exists a sufficient condition (Aly 1990): $\alpha_0 L \leqslant 1$, where α_0 is the order of magnitude of the force-free function, and L is the typical length scale of the structure. Applying this condition to the TFR with $\alpha_0 = [0.20\,; 0.55\,]$ Mm^{-1} (taken at the footpoints of the TFR in the negative polarity) and $L = 78$ Mm, we find that this condition is not fulfilled: $\alpha_0 L = [15.6\,; 42.9\,] > 1$. However, since it is only a sufficient condition for stability, we cannot conclude that the configuration is an unstable configuration. Thus, this question still remains to be addressed.

A practical way for addressing this issue thus consists in starting from the configuration reconstructed above with XTRAPOL as an initial state and solving an MHD evolution boundary value problem associated with an MHD viscous relaxation. This corresponds to a linear stability evolution in which the perturbation arises from the numerical noise. In cylindrical geometry, this would be equivalent to a superposition of various modes. Using the code METEOSOL (Amari et al. 2000), the configuration evolves ideally (i.e., with zero resistivity) from $t = 0$ to $t = 450$ in unit of Alfvén time. The various magnetic energies, the relative helicity, and the force-free parameters of the relaxed state are summarized in the last row of Table 1. At the end, the magnetic energy and the relative helicity have slightly decreased (respectively 0.3% and 3.4%). The relaxed configuration in the neighborhood of the TFR still exhibits the same three-part structure and topological features (not shown here). Moreover, the viscous relaxation had the effect of decreasing the CWsin parameter; that is, to align in a better way the current density to the magnetic field by dissipating the residual Lorentz forces. Thus, the reconstructed configuration can be considered as a linearly stable equilibrium up to those "numerical perturbations."

Although this relaxation process is not meaningful in realistic solar conditions, it agrees with the observed stability of the filament shape and with the few activities observed in the following days.

4.5. Large-scale Properties

We now study some large-scale properties of the reconstructed configuration, attempting to link them to the major features of AR 10953.

We first compare the vertically integrated current density with the *Hinode*/XRT images in Figure 5. The vertically integrated current density does not represent the real soft X-ray emission, but it may be used as a good proxy for a qualitative comparison. The X-ray telescope (XRT) image has been time averaged over the period of scan of SOT/SP. We found a strong concentration of current in the south of the AR similar to the soft X-ray emission present in the XRT image. However, neither the most southern thin structures nor the northern structures are well recovered. This could be expected as a result of the absence of information about the transverse magnetic field in the MDI data.

On the other hand, the reconstructed TFR seems to coincide with the location of the filament. To determine more precisely whether the TFR is the filament, the magnetic dips in the vicinity of the TFR have been computed.

A magnetic dip is a concavity of the magnetic field line within which the matter can be stored on a pressure scale height h. One has to find the location where $\mathbf{B}_t \cdot \nabla B_z|_{B_z=0} \geqslant 0$ (Aulanier & Demoulin 1998) and to trace the field lines from their bottom to the height h (assumed here to be 300 km). The result is shown in Figure 6 where two Hα images from *SMART* are present to compare. A quite good agreement is found between the location of magnetic dips and the darker zone on Hα images representing the filament spine. In any NLFF model, these dips are not created by gravity but are only the consequence of the current density flowing along the field lines.

Despite the presence of the sheared arcades on the "few gridpoints" of the lower part of the simulation domain, the reconstruction has shown a good correspondence with the XRT and Hα images, in addition to good force-free parameters. So, it seems that their presence below the TFR does not call into question the presence and the large-scale properties of the TFR.

5. COMPARISON WITH THE FLUX ROPE INSERTION METHOD

We now compare our results with that of Su et al. (2009) on May 2, beginning by the TFR shape. Comparing their Figure 7 with our Figure 3(c), one can see that the two TFRs are very

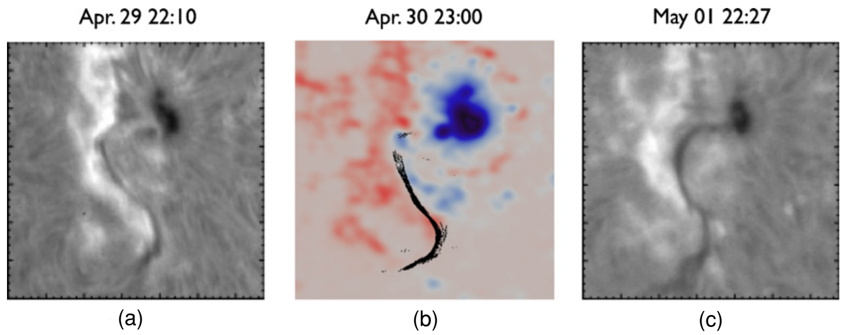

Figure 6. Comparison between *SMART*/Hα images and the location of dips in the TFR. (a) *SMART*/Hα image on 2007 April 29 at 22:10 UT, (b) location of dips from XTRAPOL, and (c) *SMART*/Hα image on 2007 May 1 at 22:27 UT.

(A color version of this figure is available in the online journal.)

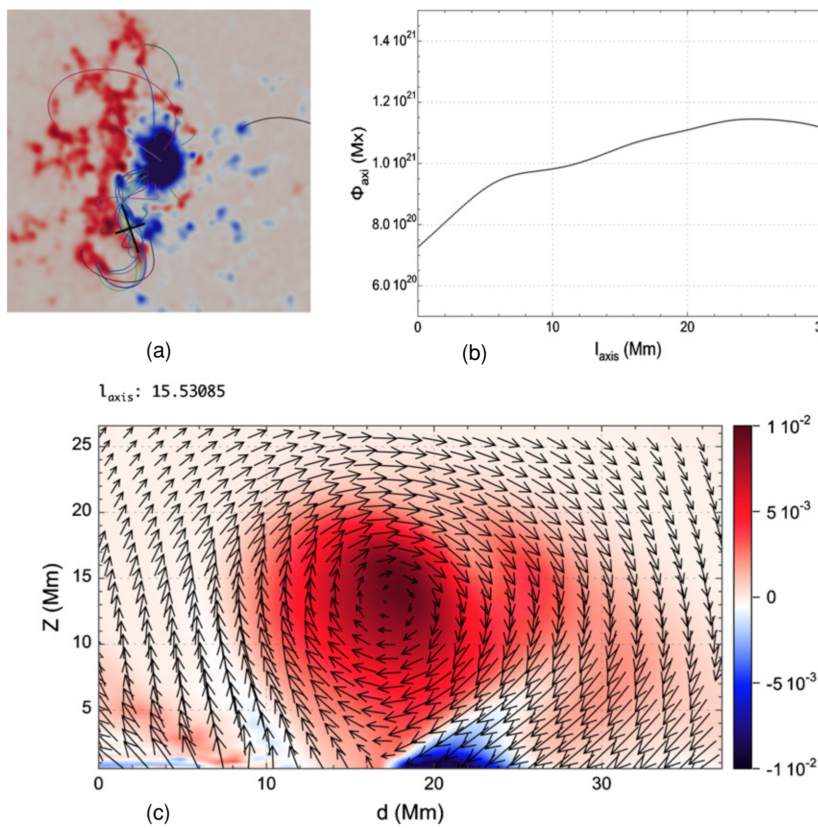

Figure 7. (a) Same figure as Figure 3(c). Black lines represent the axis along which Φ_{axi} has been computed and the transversal cut perpendicular to this axis. (b) Axial flux Φ_{axi} in Mx along the TFR. (c) Vertical cross section of the current density parallel to the TFR axis and black arrows are the transverse magnetic field.

(A color version of this figure is available in the online journal.)

similar in their structure and by the location of their anchoring footpoints. This turns out to be in agreement with both the low activity of the AR and the few changes in the filament shape as noticed by Okamoto et al. (2009) during this period. However, the TFR found by XTRAPOL seems to be more twisted.

Unlike the NLFF models, the aim of the flux rope insertion method is not to recover the features of vector magnetograms. Rather, two parameters are fixed by the user to determine the shape of the TFR: the axial flux Φ_{axi} and the poloidal flux F_{pol}. The result is then compared with the observations to determine one or several best-fit models. The axial flux Φ_{axi} for the XTRAPOL model has been computed along the straight part of the TFR axis as shown by the longest black line in Figure 7(a). As shown in Figure 7(b), the values of Φ_{axi} lie between 7×10^{20} and 12×10^{20} Mx. These values correspond to the range of values of the best-fit models of Su et al. (2009) and are below the limit of 15×10^{20} Mx above which they found the TFR to be unstable. Moreover, on each extremity of the axis chosen for the calculation, the flux starts decreasing from the location where the field lines begin to curve to connect to the photosphere.

Su et al. (2009) found a free magnetic energy of about 0.85×10^{32} erg whereas we found 2.64×10^{32} erg. These values seem consistent: on the one hand, our TFR is more twisted and, on the other hand, our model takes also into account the electrical currents outside the TFR location.

One last point which is worth comparing is the location of the current density parallel to the TFR axis in the two models. Su et al. (2009) found that it is distributed on the outer edge of the TFR. A transversal cut of the TFR axis was taken along the shortest black line in Figure 7(a). Figure 7(c) shows the current density parallel to this plane for the XTRAPOL model, and the black arrows represent the magnetic field tangent to this plane. In our model, the current is located in the core of the TFR. This might be the most striking difference between these two studies which can be however expected: in our case, the TFR is anchored in the negative polarity where a large amount of electric current is present and, in an NLFF model, the current density is located along the field lines. This also explains why a more twisted flux rope is recovered for the XTRAPOL model. However, increasing the poloidal flux F_{pol} for the flux rope insertion method leads to a current located in the core (Bobra et al. 2008), but also to possible unstable configurations.

Okamoto et al. (2008, 2009) noticed that the changes in the shape of the filament were closely related to the period of emergence of the TFR during April 28 and 29. They also observed the appearance of brightenings in the Hα images due to reconnection and they suggested that the emerging TFR reconnected with the overlying magnetic structure supporting the filament to form a single magnetic structure. The conclusion drawn by these observations is in agreement with our reconstruction models: the filament is recovered by a single TFR and there is no other dipped magnetic structure in its vicinity. However, the NLFF models cannot give any clues about the physical processes involved in the filament formation or evolution.

6. CONCLUSION

AR 10953 was a low-flaring AR during its appearance on the disk from 2007 April 26 to May 9. It presented features of an emergence of a TFR linked to the evolution of an overlying filament (Okamoto et al. 2008, 2009).

Using the vector magnetogram of *Hinode*/SOT/SP on 2007 April 30, two different numerical implementations of the Grad–Rubin algorithm have been applied to AR 10953 in order to reconstruct the 3D NLFF magnetic field. Both models highlighted the presence of a TFR above the southern part of the PIL in agreement with the location of the filament. Although they found very similar results for the magnetic configuration and the energetic content, they were able to recover the vector magnetogram features under the TFR up to the presence of small sheared arcades. This is certainly due to a combination of the following: (1) the lack of information on the MDI data and (2) underlying physical processes which imply a magnetic field too far from the NLFF assumption.

However, the force-free parameters and the viscous relaxation process confirm that the reconstructed configuration is the only one in that neighborhood and might represent a linearly stable force-free equilibrium (up to those noise level numerical perturbations). Furthermore, the magnetic dips and the vertically integrated current density have been computed and are in good agreement with the *SMART*/Hα and *Hinode*/XRT images, respectively.

These large-scale properties of the reconstructed TFR along with the independent studies of Okamoto et al. (2008, 2009) and Su et al. (2009) indicate that the cool material of the filament is supported by a TFR during a period of several days without any violent CMEs. Moreover, the free magnetic energy is already large enough to power the two C-class flares that happen during the following days.

Along with the work of Régnier & Amari (2004) and Guo et al. (2010), this work is the third example of an AR filament recovered by a TFR directly by using the whole information contained in vector magnetograms (of course, there exists other examples where different techniques from the NLFF reconstruction have been used). However, we do not claim that the magnetic structure of an AR filament is necessarily a TFR; moreover, the distinction between moderate/small twist and shear becomes disputable for arbitrary 3D magnetic configurations. And although these works are encouraging, many more ARs need to be studied with the help of both observations and NLFF modeling in order to link observable properties and evolution of ARs with their 3D magnetic configuration.

We thank P. Démoulin, T. Török, and G. Valori for valuable discussions about this AR, and M. DeRosa for his explanations about co-alignment of XRT images, as well as G. Aulanier for more general stimulating discussions. *Hinode* is a Japanese mission developed and launched by ISAS/JAXA, with NAOJ as a domestic partner, and NASA and STFC (UK) as international partners. It is operated by these agencies in co-operation with ESA and NSC (Norway). We also thank CNES (Centre National d'Etudes Spatiales) for support.

REFERENCES

Aly, J. J. 1989, Sol. Phys., 120, 19
Aly, J. J. 1990, Phys. Fluids B, 2, 1928
Aly, J. J. 1991, ApJ, 375, 61
Aly, J. J., & Amari, T. 1989, A&A, 221, 287
Aly, J. J., & Amari, T. 2007, Geophys. Astrophys. Fluid Dyn., 101, 249
Amari, T., & Aly, J. J. 1989, A&A, 208, 261
Amari, T., & Aly, J. J. 1992, A&A, 265, 791
Amari, T., Aly, J. J., Luciani, J. F., Boulmezaoud, T. Z., & Mikic, Z. 1997, Sol. Phys., 174, 129
Amari, T., Aly, J. J., Mikic, Z., & Linker, J. 2007, ApJ, 671, L189
Amari, T., Boulmezaoud, T. Z., & Aly, J. J. 2006, A&A, 446, 691
Amari, T., Luciani, J. F., & Aly, J. J. 2004, ApJ, 615, L165
Amari, T., Luciani, J. F., & Aly, J. J. 2005, ApJ, 629, L37
Amari, T., Luciani, J. F., Aly, J. J., Mikic, Z., & Linker, J. 2003a, ApJ, 585, 1073
Amari, T., Luciani, J. F., Aly, J. J., Mikic, Z., & Linker, J. 2003b, ApJ, 595, 1231
Amari, T., Luciani, J. F., Mikic, Z., & Linker, J. 1999, ApJ, 518, L57
Amari, T., Luciani, J. F., Mikic, Z., & Linker, J. 2000, ApJ, 529, L49
Antiochos, S. K., DeVore, C. R., & Klimchuk, J. A. 1999, ApJ, 510, 485
Anzer, U., & Priest, E. 1985, Sol. Phys., 95, 263
Archontis, V., Moreno-Insertis, F., Galsgaard, K., Hood, A., & O'Shea, E. 2004, A&A, 426, 1047
Aulanier, G., & Demoulin, P. 1998, A&A, 329, 1125
Aulanier, G., DeVore, C. R., & Antiochos, S. K. 2002, ApJ, 567, L97
Aulanier, G., Török, T., Démoulin, P., & DeLuca, E. E. 2010, ApJ, 708, 314
Bleybel, A., Amari, T., van Driel-Gesztelyi, L., & Leka, K. D. 2002, A&A, 395, 685
Bobra, M. G., van Ballegooijen, A. A., & DeLuca, E. E. 2008, ApJ, 672, 1209
Boulmezaoud, T. Z., & Amari, T. 2000, Z. Angew. Math. Phys., 51, 942
Canou, A., Amari, T., Bommier, V., Schmieder, B., Aulanier, G., & Li, H. 2009, ApJ, 693, L27
Cheung, M. C. M., Schüssler, M., & Moreno-Insertis, F. 2007, A&A, 467, 703
Cuperman, S., Demoulin, P., & Semel, M. 1991, A&A, 245, 285
Démoulin, P. 1998, in ASP Conf. Ser., 150, IAU Colloq. 167, New Perspectives on Solar Prominences, ed. D. F. Webb, B. Schmieder, & D. M. Rust (San Francisco, CA: ASP), 78
Démoulin, P., & Priest, E. R. 1988, A&A, 206, 336
Démoulin, P., & Priest, E. R. 1989, A&A, 214, 360
DeRosa, M. L., et al. 2009, ApJ, 696, 1780
DeVore, C. R., & Antiochos, S. K. 2000, ApJ, 539, 954
Dudík, J., Aulanier, G., Schmieder, B., Bommier, V., & Roudier, T. 2008, Sol. Phys., 248, 29
Fan, Y. 2001, ApJ, 554, L111
Fan, Y., & Gibson, S. E. 2004, ApJ, 609, 1123
Finn, J. H., & Antonsen, T. M. 1985, Comments Plasma Phys. Control. Fusion, 9, 111
Galsgaard, K., Moreno-Insertis, F., Archontis, V., & Hood, A. 2005, ApJ, 618, L153

Gary, G. A., & Moore, R. L. 2004, ApJ, 611, 545
Grad, H., & Rubin, H. 1958, in Proc. 2nd Intern. Conf. Peaceful Uses of Atomic Energy, Vol. 31 (Geneva: United Nations), 190
Guo, Y., Schmieder, B., Démoulin, P., Wiegelmann, T., Aulanier, G., Török, T., & Bommier, V. 2010, ApJ, 714, 343
Kuperus, M., & Raadu, M. A. 1974, A&A, 31, 189
Lionello, R., Mikić, Z., Linker, J. A., & Amari, T. 2002, ApJ, 581, 718
López Fuentes, M. C., Demoulin, P., Mandrini, C. H., & van Driel-Gesztelyi, L. 2000, ApJ, 544, 540
Lynch, B. J., Antiochos, S. K., DeVore, C. R., Luhmann, J. G., & Zurbuchen, T. H. 2008, ApJ, 683, 1192
Mackay, D. H., Karpen, J. T., Ballester, J. L., Schmieder, B., & Aulanier, G. 2010, Space Sci. Rev., 151, 333
Magara, T., & Longcope, D. W. 2003, ApJ, 586, 630
Manchester, W., IV, Gombosi, T., DeZeeuw, D., & Fan, Y. 2004, ApJ, 610, 161
McClymont, A. N., Jiao, L., & Mikic, Z. 1997, Sol. Phys., 174, 191
Metcalf, T. R., et al. 2006, Sol. Phys., 237, 267
Okamoto, T. J., et al. 2008, ApJ, 673, L215
Okamoto, T. J., et al. 2009, ApJ, 697, 913
Pevtsov, A. A., Canfield, R. C., & Latushko, S. M. 2001, ApJ, 549, L261
Pevtsov, A. A., Canfield, R. C., & Metcalf, T. R. 1995, ApJ, 440, L109
Régnier, S., & Amari, T. 2004, A&A, 425, 345
Scherrer, P. H., et al. 1995, Sol. Phys., 162, 129
Schrijver, C. J., et al. 2006, Sol. Phys., 235, 161
Sturrock, P. A. 1991, ApJ, 380, 655
Su, Y., van Ballegooijen, A., Lites, B. W., Deluca, E. E., Golub, L., Grigis, P. C., Huang, G., & Ji, H. 2009, ApJ, 691, 105
Titov, V. S. 2007, ApJ, 660, 863
Titov, V. S., & Démoulin, P. 1999, A&A, 351, 707
Titov, V. S., Hornig, G., & Démoulin, P. 2002, J. Geophys. Res., 107, 1164
Titov, V. S., Priest, E. R., & Démoulin, P. 1993, A&A, 276, 564
Tsuneta, S., et al. 2008, Sol. Phys., 249, 167
van Ballegooijen, A. A. 2004, ApJ, 612, 519
van Ballegooijen, A. A., DeLuca, E. E., Squires, K., & Mackay, D. H. 2007, J. Atmos. Terr. Phys., 69, 24
van Ballegooijen, A. A., & Martens, P. C. H 1989, ApJ, 343, 971
Wheatland, M. S., Sturrock, P. A., & Roumeliotis, G. 2000, ApJ, 540, 1150
Wiegelmann, T. 2008, J. Geophys. Res., 113, A03S02
Wiegelmann, T., Inhester, B., & Sakurai, T. 2006, Sol. Phys., 233, 215